Journal of Physics B: Atomic, Molecular and Optical Physics

The coupled system $(2)^2\Sigma^+$ and $(1)^2\Pi$ of $^7Li^{88}Sr$

OPEN ACCESS
IOP Publishing
Journal of Physics B: Atomic, Molecular and Optical Physics
J. Phys. B: At. Mol. Opt. Phys. **53** (2020) 065102 (10pp)
https://doi.org/10.1088/1361-6455/ab68f8

The coupled system $(2)^2\Sigma^+$ and $(1)^2\Pi$ of $^7Li^{88}Sr$

Erik Schwanke[1,2,3], Julia Gerschmann[1,2], Horst Knöckel[1,2], Silke Ospelkaus[1,2] and Eberhard Tiemann[1,2]

[1] Leibniz Universität Hannover, Institute of Quantum Optics, Welfengarten 1, D-30167, Hannover, Germany
[2] Leibniz Universität Hannover, Laboratory for Nano- and Quantum Engineering, Schneiderberg 39, D-30167, Hannover, Germany

E-mail: schwanke@iqo.uni-hannover.de and tiemann@iqo.uni-hannover.de

Received 27 November 2019, revised 10 December 2019
Accepted for publication 8 January 2020
Published 4 March 2020

Abstract

We analyse rovibrational transitions of the $(2)^2\Sigma^+$–$X(1)^2\Sigma^+$ system of LiSr and find the energy levels of the $(2)^2\Sigma^+$ state to be perturbed by coupling between the $(2)^2\Sigma^+$ and $(1)^2\Pi$ states. We present an analysis of the coupled system yielding molecular parameters for the lowest vibrational levels of the $(2)^2\Sigma^+$ state and for higher vibrational levels of the $(1)^2\Pi$ state together with molecular coupling constants. Improved Dunham coefficients for the rovibrational levels of the $X(1)^2\Sigma^+$ state are also obtained, where the correlation with the parameters of the excited states is removed completely.

Supplementary material for this article is available online

Keywords: rotation, vibration and vibration–rotation constants, molecular spectra, potential energy surfaces

(Some figures may appear in colour only in the online journal)

1. Introduction

In the last decade, much research on the energy structure of molecules consisting of one alkali and one alkaline earth atom has been conducted with the aim to produce ultracold samples of such molecules (see e.g. [1–5]). There are proposals to use these open-shell molecules for precision measurements [6], to study scattering phenomena of ultracold particles [7] and dipolar interactions [8].

There exist *ab initio* calculations [1, 9–14] of potential energy curves of several electronic states of LiSr and transition probabilities between its electronic ground state and excited states. These data are very useful guides for spectroscopic studies, which then will yield the desired accurate molecular parameters for the experiments with ultracold ensembles.

We previously investigated the near infrared spectrum of $^7Li^{88}Sr$ and derived Dunham coefficients for the lowest vibrational levels of the $X(1)^2\Sigma^+$ and $(2)^2\Sigma^+$ states [15]. Figure 1 shows the electronic states in the observed spectral range. We observed perturbations in the $(2)^2\Sigma^+$ energy levels and used a coupled-state model for the $(2)^2\Sigma^+$ and $(1)^2\Pi_{1/2}$ states to explain a strong perturbation in the (0–0) band of rotational angular momenta up to $N = 65$, while neglecting the weaker coupling with the $(1)^2\Pi_{3/2}$ state.

Here, we now present an extensive study of the perturbations in the first two vibrational levels of the $(2)^2\Sigma^+$ state for $N \leqslant 119$. These perturbations allow to find a consistent description of the $\Omega = 1/2$ and $\Omega = 3/2$ components of six vibrational levels in the $(1)^2\Pi$ state. Our extended model also gives improved Dunham coefficients for the $^2\Sigma^+$ states and molecular coupling constants compared to our previous work.

2. Experimental work and quantum number assignment

For spectroscopy, the molecular sample was produced in a heat pipe in the same way as described in our previous work

[3] Author to whom any correspondence should be addressed.

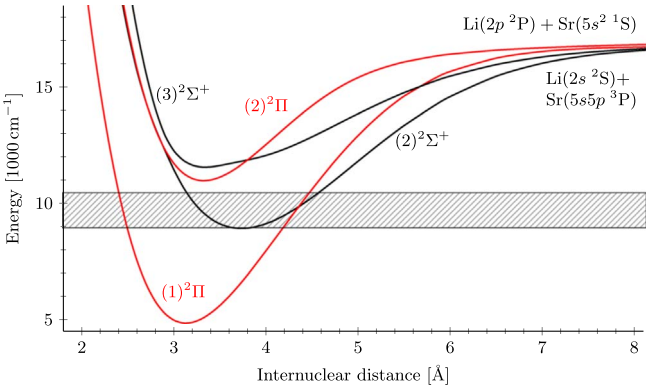

Figure 1. *Ab initio* potential energy curves [16] of the doublet manifold of LiSr corresponding to the singly excited atomic states. The hatched region indicates the energy range of the observed NIR spectrum of the $(2)^2\Sigma^+$–$X(1)^2\Sigma^+$ system. The perturbation of $(2)^2\Sigma^+$ levels is explained by the coupling to the $(1)^2\Pi$ state.

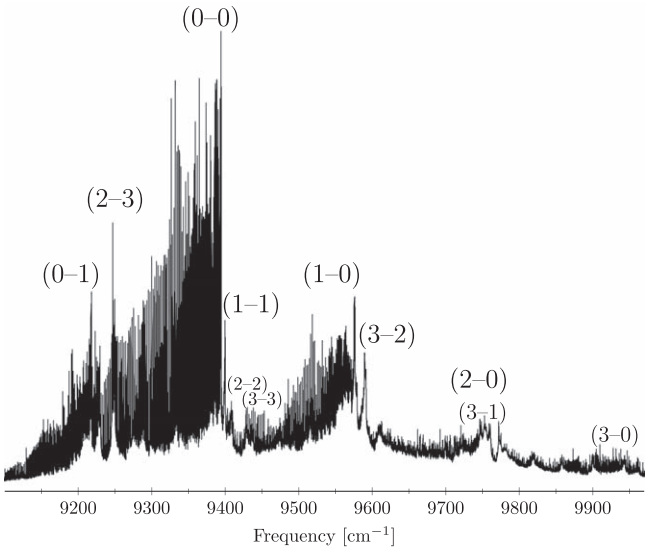

Figure 2. Thermal emission spectrum of LiSr in the near-infrared spectrum. Vibrational bands with v up to 3 are indicated, where distinctly visible.

[15]. We recorded the thermal emission spectrum and laser-induced fluorescence (LIF) spectra. The thermal emission spectrum of LiSr is shown in figure 2 with assignments of vibrational bands. These assignments are an extrapolation from our modelled system (see section 5), which incorporates only $v'' = 0$, 1, 2 for $X(1)^2\Sigma^+$ and $v' = 0$, 1 for $(2)^2\Sigma^+$. The shapes and positions of band structures simulated with our findings are in good agreement with the observed spectrum. We only assigned the spectrum of $^7Li^{88}Sr$, the spectra of other isotopologues are too weak to be identified in our recorded spectrum. The LIF spectra show certain transition lines with a higher intensity as in the pure thermal emission spectrum. These exaggerations tell which lines in the dense thermal emission spectrum have a common upper level. Rotational lines from the P ($N'' = N' + 1$) and R ($N'' = N' - 1$) branches with the same upper level N' were identified by this method. The frequency difference between a PR line pair together with the ground state rotational constant B_v'' allow to

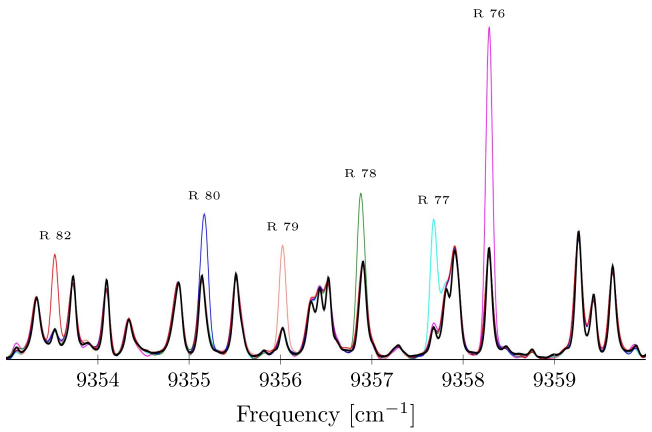

Figure 3. Fluorescence lines (from different LIF experiments, each in a different colour) in the F_1 R branch of the (1–1) band with rotational quantum number N'' plotted together with the thermal emission spectrum (black). The shown thermal emission lines are explained with our model, except some of the weak ones. This picture is a composition of several LIF spectra with excitations in the P branch. The fluorescence and thermal emission spectra were recorded with different resolutions, which leads to different line shapes. The fluorescence shows some (1–1) lines otherwise hidden by the more intense (0–0) spectrum. Thus, the centres of some fluorescence lines do not coincide with the centres of the thermal emission lines. Those positions of the (1–1) lines could only be read from the LIF spectrum.

unambiguously assign the rotational quantum numbers to the lines. The LIF spectra further highlight lines with the same rotational quantum numbers in other vibrational bands following a vibrational progression. For an illustration, figure 3 shows LIF lines of the F_1 R branch of the (1–1) band. (F_1 or F_2 label the spin-rotation doublets of rotational state N as defined at the end of this section.) They result from laser excitations in the P branch of the same band around 9300 cm^{-1}. The fluorescence lines (coloured) have a higher intensity than the corresponding ones in the thermal emission spectrum (black). We used the frequency difference of the P and R lines together with the rotational constant of the electronic ground state to find the quantum numbers of the excited and answering lines. The same excitations also yield fluorescence in the (1–0) band, at frequencies from 9440 to 9520 cm^{-1} (see figure 2), as well as PR pairs in the (1–2) band (not labelled in figure 2). The (1–1) band is mostly obscured by the more intense (0–0) band, so that many (1–1) lines cannot reliably be identified in the thermal emission spectrum. However, their frequencies can be determined from the LIF spectra despite the strong overlap of the (0–0) band. For the lines F_1 R 78 and 80, the fluorescence shows a visibly different central frequency than the line structure in the thermal emission spectrum.

Because of the shape and very similar equilibrium positions of the potentials of the $X(1)^2\Sigma^+$ and $(2)^2\Sigma^+$ states in alkali-alkaline earth diatomics, vibrational bands with large differences in the vibrational quantum number have small Franck–Condon factors [13]. Therefore, only short progressions are expected and in the actual case only the $v'' = 0$, 1, 2

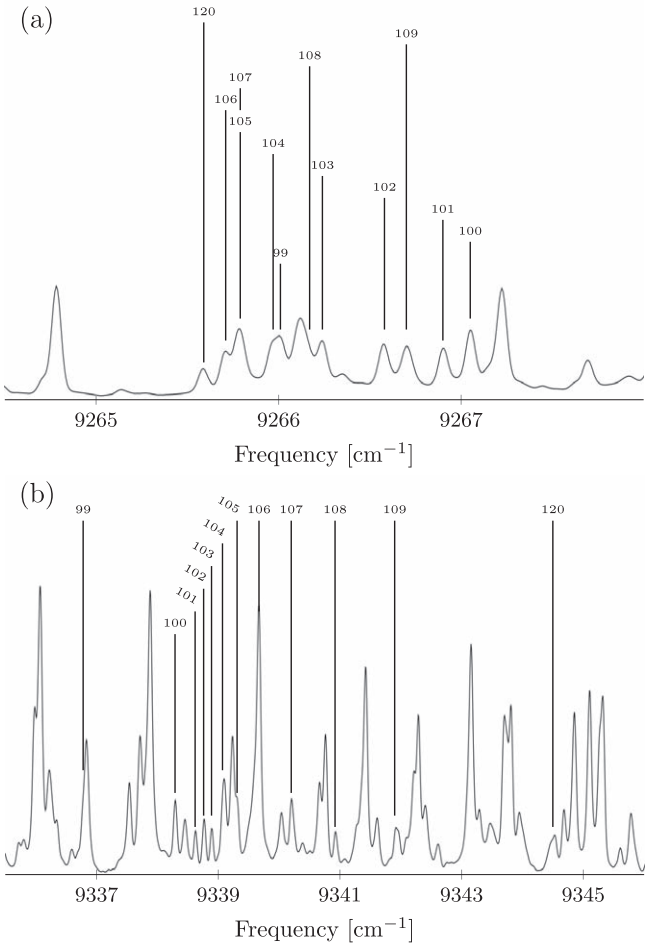

Figure 4. Line assignments of F_1 (1–1) lines by fluorescence experiments for strongly perturbed spectral ranges in the thermal emission spectrum. For LIF experiments, the laser was tuned to the frequencies marked in (a) and fluorescence was seen at the frequencies indicated by the vertical lines in (b). Each excited line has a corresponding fluorescence line marked by the same quantum number N'. The clear structure of the LIF spectra allowed to identify PR pairs from the lines in (a) and (b). The thermal emission lines in (a) and (b) are finally all assigned within our analysis, except some of the weak ones.

levels of the $X(1)^2\Sigma^+$ state could be detected by laser excitation of $v' = 0$, 1 levels of the $(2)^2\Sigma^+$ state.

We observed that the frequencies of transition lines deviate from a regular rovibrational energy structure for many $(2)^2\Sigma^+$ levels. These deviations were too large to convincingly identify the quantum numbers from the rotational series in the thermal emission spectrum. Moreover, the intensity of the strongly perturbed lines dropped considerably, which further hindered the tracking of a rotational branch in the spectrum. Here, the LIF experiments in the perturbed parts of rotational branches helped to determine rotational quantum numbers of unknown spectral lines in small steps. By this approach, we were able to identify and assign lines with a large frequency shift and thus gather data about the perturbations in the $(2)^2\Sigma^+$ state. Figure 4 shows the F_1 P and R branches of the (1–1) band for $N' \geqslant 99$. These lines are mostly discernible in the thermal emission spectrum but much weaker than the surrounding (0–0) lines. Excitations at the frequencies indicated in figure 4(a) lead to fluorescence at the frequencies marked in figure 4(b). The $(2)^2\Sigma^+$ levels corresponding to the excitations are strongly perturbed (see figure 6 later). This perturbation heavily disorganizes the order of the lines. In figure 4(a), it describes a zigzag pattern when following N'. Here again the LIF spectra allowed us to quickly identify the correct quantum numbers, which together with the line frequencies showed us the development of the perturbation. The lines with $N' = 120$ in figure 4 could be assigned via their PR distance but the derived level energies could not be included in the fit, because the gap to the systematically recorded rotational ladder is too big and probably contains the next strongly perturbed region (see figure 6).

The rotational ladder for $v' = 0$ could be followed up to $N' = 115$ and that for $v' = 1$ from $N' = 40$ to $N' = 109$. Especially for $v' = 1$, we could not completely follow the series to the perturbation centres because the lines became too weak due to the strong coupling.

All observed transitions belong to the $(2)^2\Sigma^+$–$X(1)^2\Sigma^+$spectrum and no transition to the neighbouring state $(1)^2\Pi$ (see figure 1) was found. Our description of the $(1)^2\Pi$ state, derived from the coupling to the $(2)^2\Sigma^+$ state (see below), is confined to a few vibrational levels around $v_\Pi = 14$ according to *ab initio* calculations [11, 13]. With those data, it is not possible to accurately extrapolate to lower $(1)^2\Pi$ levels. We tried to directly observe the $(1)^2\Pi$–$X(1)^2\Sigma^+$ spectrum, which the *ab initio* calculations predict around 5000 cm^{-1}, using an InGaAs avalanche photodiode (G8931-20, Hamamatsu). We did not observe any spectrum in the region from 5000 to 9000 cm^{-1}. Reasons are: (1) the InGaAs detector is less responsive and noisier than the Si-APD we used to observe the $(2)^2\Sigma^+$–$X(1)^2\Sigma^+$ spectrum (S11519-30, Hamamatsu) and (2) the molecular transitions are much weaker than those of the observed $(2)^2\Sigma^+$–$X(1)^2\Sigma^+$ spectrum according to the *ab initio* calculations [11, 13].

Our previous, simplified analysis [15], which neglected the $(1)^2\Pi$ spin-orbit-coupling, was performed in Hund's coupling case (b). The basis vector in this case is $|\Lambda, (N, S)J\rangle$ with the quantum numbers of the projection of the orbital angular momentum onto the molecular axis, Λ, the total angular momentum without spins, $\hat{N}$, the electronic spin $\hat{S}$ and the total angular momentum without nuclear spins, $\hat{J} = \hat{N} + \hat{S}$. We used Dunham coefficients for the rovibrational energy description in both electronic states, so that the energies for Σ states can be expressed as

$$E^{(b)}_{Dun}(v, N) = \sum_{m,n} Y^{(b)}_{m,n}[v + 1/2]^m [N(N+1)]^n. \qquad (1)$$

Due to the coupling between the electronic spin and the nuclear rotation, the rovibrational energy levels in a $^2\Sigma^+$ state are split. The levels for which $J = N + 1/2$ are called F_1 levels and have *e*-type symmetry. The levels for which $J = N - 1/2$ are called F_2 levels and have *f*-type symmetry (see section 2.2.2 in [17]). The spin-rotation energy E_{SR} from $\hat{H}_{SR} = \gamma\hat{S}\hat{N}$ is simply added to the rovibrational energy because this operator is diagonal in the quantum numbers N

Table 1. Derived Dunham and spin-rotation parameters for levels with $N \leqslant 115$ for $v = 0$, 1 and $40 \leqslant N \leqslant 63$ for $v = 2$ of the ground state $X(1)^2\Sigma^+$. The uncertainties are those derived in the linear fit (resulting in $\sigma = 0.25$, see text). All values are given in cm^{-1} and are valid for $^7\mathrm{Li}^{88}\mathrm{Sr}$.

Y_{0n}	Y_{1n}	Y_{2n}	γ_{0n}	γ_{1n}	n
0.00(1)	$1.830\,781(39) \times 10^{2}$	$-3.1018(17) \times 10^{0}$	$8.18(37) \times 10^{-3}$	$-5.04(11) \times 10^{-4}$	0
$2.074\,024(45) \times 10^{-1}$	$-3.4164(18) \times 10^{-3}$	$-5.724(78) \times 10^{-5}$	—	—	1
$-1.083\,17(50) \times 10^{-6}$	$-3.540(19) \times 10^{-8}$	$-6.628(71) \times 10^{-9}$	—	—	2
—	—	—	—	—	3
$-2.309(15) \times 10^{-16}$	$-1.1953(51) \times 10^{-16}$	—	—	—	4

and S. It reads with the spin-rotation coupling constant γ as

$$E_{\mathrm{SR}} = \pm\frac{\gamma}{2}\,[N + 1/2 \mp 1/2] = -\frac{\gamma}{2}\,[1 \mp (J + 1/2)], \tag{2}$$

where the upper sign is for F_1 and the lower sign for F_2 levels. We expressed γ itself with a Dunham-like expansion to include a dependence on the rovibrational motion:

$$\gamma(v, N) = \sum_{m,n} \gamma_{m,n}(v + 1/2)^m [N(N + 1)]^n. \tag{3}$$

3. Ground state analysis

The lines addressed with the LIF experiments covered ground state levels with $v'' = 0$, 1, 2 and $N'' \leqslant 115$. The frequency differences between fluorescence and/or laser lines in a LIF spectrum correspond to energy differences in the $X(1)^2\Sigma^+$ state. These are independent of perturbations in the excited state and will suppress the correlations between upper and lower state parameters typically obtained from the fit of optical transition frequencies. We chose a minimum uncertainty of $0.02\,\mathrm{cm}^{-1}$ that is slightly less than the Doppler broadening of $0.024\,\mathrm{cm}^{-1}$. Thus we take into account that we are limited by the observed thermal emission spectrum when setting the laser frequency to a transition line. We conducted a linear fit of Dunham and spin-rotation coupling parameters according to equations (1)–(3) to the frequency differences. This fit gave a weighted standard deviation of $\sigma = 0.25$, with 99.64% of data being modelled within their assumed uncertainty. The low value of σ indicates that we could have assumed a smaller minimum uncertainty which shows that setting the laser on resonance was typically better than within the Doppler width. The fitted coefficients and their standard deviations are given in table 1. Calculating ground state energies with these parameters will have an uncertainty of at least that of the absolute accuracy of the frequency scale, i. e. $0.01\,\mathrm{cm}^{-1}$.

We applied the derived molecular parameters of the ground state to construct the level system of the perturbed state $(2)^2\Sigma^+$ from the measured transition frequencies. Now the data for the $X(1)^2\Sigma^+$ and $(2)^2\Sigma^+$ levels are independent of each other as long as the assignment is correct. The uncertainties of the constructed $(2)^2\Sigma^+$ levels are composed of the uncertainties of the ground state levels and the uncertainty of a spectral line. We chose a minimum uncertainty of $0.02\,\mathrm{cm}^{-1}$ for the constructed levels, but most levels of the state $(2)^2\Sigma^+$ have an uncertainty of $0.03\,\mathrm{cm}^{-1}$.

4. The coupled system $(2)^2\Sigma^+$ –$(1)^2\Pi$

For the joint description of the $(2)^2\Sigma^+$ and $(1)^2\Pi$ level systems and their coupling, we apply Hund's coupling case (a) with the state vector $|\Lambda, S, \Sigma, J, e/f\rangle$ because the $^2\Pi$-state with its significant spin-orbit interaction [11] is close to this coupling case. Here, Λ and Σ are the quantum numbers of the projections of the electronic orbital angular momentum and the spin onto the molecular axis and $\Omega = \Lambda + \Sigma$ is defined as the projection of the total angular momentum $\hat{J}$ excluding nuclear spins. The terms in the Dunham energies have to be adapted for this coupling case. For $^2\Sigma^+$ levels, they are given by

$$E^{(\mathrm{a})}_{\mathrm{Dun}}(v, J, e/f) = \textstyle\sum_{m,n} Y^{(\mathrm{a})}_{m,n}[v + 1/2]^m \times [(J \mp 1/2)(J \mp 1/2 + 1)]^n \tag{4}$$

with the upper sign for e (F_1) levels and the lower sign for f (F_2) levels. With this convention, equations (1) and (4) have equal parameters in Hund's cases (a) and (b). For $^2\Pi$ levels, the energy is given by

$$E^{(\mathrm{a})}_{\mathrm{Dun}}(v, J) = \textstyle\sum_{m,n} Y^{(\mathrm{a})}_{m,n} \times [v + 1/2]^m \begin{cases} [(J)(J + 1) + 1/4]^n & \text{for } ^2\Pi_{1/2} \\ [(J)(J + 1) - 7/4]^n & \text{for } ^2\Pi_{3/2}, \end{cases} \tag{5}$$

being the same for e and f levels. Similarly, the rotational constant of a vibrational level v is expressed as

$$B_{\Pi}^{(v,v)} = \sum_{m} Y^{(\mathrm{a})}_{m,1}[v + 1/2]^m. \tag{6}$$

Table 2 shows the matrix for the coupling of a $^2\Sigma^+$ state and a $^2\Pi$ state with their vibrational levels v_Σ, v_Π and v'_Π by the spin-orbit and rotational interaction with its respective molecular coupling parameters A (spin-orbit interaction) and B (rotational interaction) [17]. The rovibrational energies of the basis states are represented according to equations (4) and (5). The diagonal term for the state $(2)^2\Sigma^+$ in Hund's case (a) is exactly the value calculated with equations (1) to (3) in Hund's case (b), only expressed with the quantum numbers J and e/f.

Table 2. Matrix representation of couplings between $^2\Sigma^+$, $^2\Pi_{1/2}$ and $^2\Pi_{3/2}$ states in Hund's case (a) for a total angular momentum J. The upper and lower signs are for e and f levels, respectively. See the text for an explanation of the constants.

	$\lvert v_\Sigma,^2\ \Sigma^+_{1/2},\ e/f\rangle$	$\lvert v_\Pi,^2\ \Pi_{1/2},\ e/f\rangle$	$\lvert v'_\Pi,^2\ \Pi_{3/2},\ e/f\rangle$
$\langle v_\Sigma,^2\ \Sigma^+_{1/2},\ e/f\rvert$	$E^{\Sigma,(a)}_{\mathrm{Dun}} - \gamma_\Sigma/2 \cdot [1 \mp (J + 1/2)]$	$V_{\Sigma\Pi} \cdot p/2 \times [A_{\Sigma\Pi} - \gamma_{\Sigma\Pi} + 2B_{\Sigma\Pi}(1 \mp [J + 1/2])]$	$-V_{\Sigma\Pi} \cdot p \cdot B_{\Sigma\Pi} \times \sqrt{J(J+1) - 3/4}$
$\langle v_\Pi,^2\ \Pi_{1/2},\ e/f\rvert$	$V_{\Sigma\Pi} \cdot p/2 \cdot [A_{\Sigma\Pi} - \gamma_{\Sigma\Pi} + 2B_{\Sigma\Pi}(1 \mp [J + 1/2])]$	$E^{\Pi,(a)}_{\mathrm{Dun}} - (A_\Pi + \gamma_\Pi)/2$	$(V_\Pi \cdot \gamma_\Pi/2 - B^{(v,v')}_\Pi) \times \sqrt{J(J+1) - 3/4}$
$\langle v'_\Pi,^2\ \Pi_{3/2},\ e/f\rvert$	$-V_{\Sigma\Pi} \cdot p \cdot B_{\Sigma\Pi} \times \sqrt{J(J+1) - 3/4}$	$(V_\Pi \cdot \gamma_\Pi/2 - B^{(v,v')}_\Pi) \times \sqrt{J(J+1) - 3/4}$	$E^{\Pi,(a)}_{\mathrm{Dun}} + (A_\Pi - \gamma_\Pi)/2$

The matrix includes the spin-rotation coupling (with constant γ) resulting from 'distant' electronic states not considered in the basis system, i.e. those not included in our model. The spin-rotation from the 'local' system results from the non-diagonal term of $^2\Sigma$ and $^2\Pi_{1/2}$, which also gives the e/f-splitting of the state $(1)^2\Pi$, normally called Λ- or Ω-doubling. The subscripts Σ and Π at the parameters indicate to which electronic state(s) they belong. Because the matrix in table 2 describes the restricted Hilbert space for selected vibrational levels, the primary coupling parameters are multiplied by overlap integrals of vibrational wave functions of the $^2\Sigma^+$ and the $^2\Pi$ state ($V_{\Sigma\Pi} \coloneqq \langle v_\Sigma | v_\Pi \rangle$). Here, we neglect a dependence of the coupling parameters on the internuclear distance R. The parameter p is a shorthand for the expectation value of the ladder operator of the electronic orbital angular momentum:

$$p \coloneqq \langle \Pi | L^+ | \Sigma \rangle. \tag{7}$$

It would evaluate to $\sqrt{2}$ if the molecular states could be traced back to p-electrons, as it is true asymptotically ($R \to \infty$) for LiSr. There are no couplings between levels with different J quantum numbers because we neglect hyperfine interactions and also e/f are constants of motion; so the matrix in table 2 can be used for each observed $(2)^2\Sigma^+$ level independently.

In the non-diagonal matrix elements $\langle \Pi | ... | \Sigma \rangle$, products of parameters appear which cannot be determined separately by the fit. Thus we introduce the effective parameters:

$$V_{\Sigma\Pi}^{\text{fit}} \coloneqq V_{\Sigma\Pi} \cdot p \cdot (A_{\Sigma\Pi} - \gamma_{\Sigma\Pi}) \tag{8}$$

$$B_{\Sigma\Pi}^{\text{fit}} \coloneqq B_{\Sigma\Pi} / (A_{\Sigma\Pi} - \gamma_{\Sigma\Pi}). \tag{9}$$

The first of them is later on called simply overlap integral and the second the rotational constant. The considered matrix elements only depend on these parameters.

The value of γ_Π is generally small compared to A_Π and B_Π, therefore we disregard it. As such, only expression (3) with γ_Σ is left for the spin-rotation interaction in our model. The supplementary material (available online at stacks.iop.org/JPB/53/065102/mmedia) explains the approximation of the effective rotational constant $B_\Pi^{(v,v')} \approx \sqrt{\frac{4\,B_e^3}{\omega_e}}$ for the non-diagonal matrix element $\langle v_\Pi, ^2\Pi_{1/2} | \hat{H} | v'_\Pi, ^2\Pi_{3/2} \rangle$ for $v_\Pi \neq v'_\Pi$.

When plotting the energy levels of the $(2)^2\Sigma^+$ state derived from the observations as function of $J(J+1)$, the series of rotational energies appears as an almost straight line for each vibrational level. The slopes of these lines represent effective rotational constants. Figure 5 shows this level scheme for $v' = 0$, 1 (red and blue series of dots) and additionally the assumed rotational ladder of the $(1)^2\Pi$ state (black and green series of dots) where the crossings of both states become visible. If one redraws such plots for the directly observed $(2)^2\Sigma^+$ levels by shifting the rotational energy according to effective rotational constants, almost horizontal lines appear, where within narrow J-ranges deviations show up. These deviations indicate the perturbation and thus the crossing of the rotational ladders of the studied state (here $(2)^2\Sigma^+$) with those of the perturbing state (here $(1)^2\Pi$) more clearly. This is illustrated in figure 6, where we plotted the energy shift introduced by the coupling compared to 'unperturbed' levels calculated with the simple Dunham model. In such a plot, perturbed ranges are undoubtedly detected.

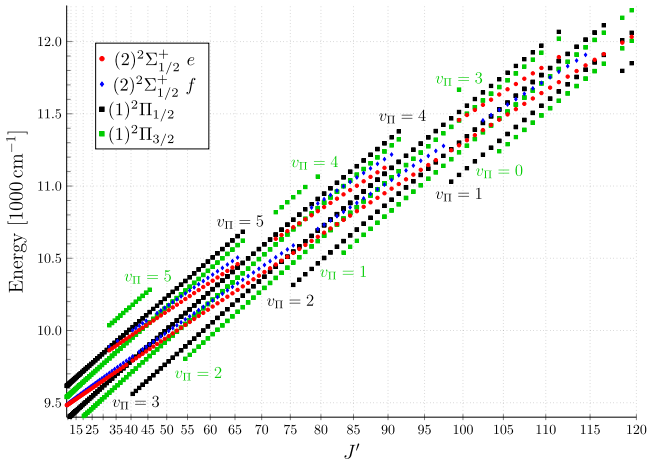

Figure 5. Constructed $(2)^2\Sigma^+$ energy levels with their surrounding $(1)^2\Pi$ levels. The J-axis is scaled by $J(J+1)$. The lowest involved vibrational level was assumed to be $v_\Pi = 0$ (see text). The crossing points of the $^2\Sigma^+$ levels and the $^2\Pi_{1/2}$ levels correspond to broad perturbations in the $(2)^2\Sigma^+$–$X(1)^2\Sigma^+$ spectrum and the $^2\Pi_{3/2}$ crossings correspond to sharp perturbations.

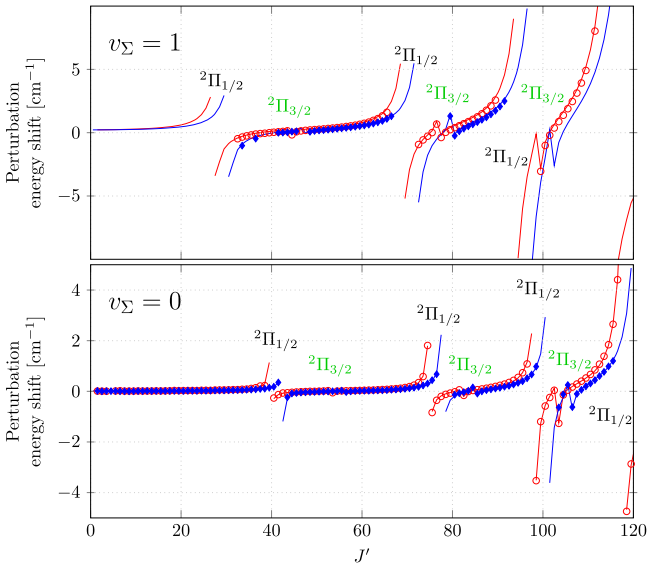

Figure 6. Energy shift of $(2)^2\Sigma^+$ levels due to the coupling to the $(1)^2\Pi$ state. There are extended regions of strong perturbations around crossing points with the $^2\Pi_{1/2}$ levels and narrow ones of weaker perturbations around crossing points with the $^2\Pi_{3/2}$ levels. The symbols (red circles for e levels and blue diamonds for f levels) represent measured data (the experimental uncertainty lies within the symbol size) and the lines are data calculated with the coupled state model. These lines are mostly hidden by the symbols.

For the nonlinear fit of the molecular parameters according to table 2, we compared each energy level with quantum numbers (v_Σ, J, e/f) constructed from the observations with the eigenvalue of the appropriate coupling matrix with the largest amplitude of the basis vector $|v_\Sigma, ^2\Sigma^+_{1/2}, e/f\rangle$. The fit was conducted with the MINUIT software [18].

As starting values for the Dunham coefficients of the state $(2)^2\Sigma^+$, we used the preliminarily obtained ones from a linear Dunham fit of those levels which could be identified as very weakly perturbed by its regular structure of the rotational energy. Four such crossings, strong deviations were observed for each of the rotational ladders. Initial energy values for the state $(1)^2\Pi$ were estimated from these crossing energies taken as approximate energies of the $\Omega = 1/2$ component of state $(1)^2\Pi$. A vibrational quantum number was assigned simply by counting from $v_\Pi = 0$ for the lowest included vibrational level. The observed energy structure of the perturbation does not contain information to establish absolute v_Π quantum numbers and our model does not use vibrational wave functions explicitly. Thus the present choice of low v_Π has no drawback for the description of the energies.

In figure 6, sharp small deviations are visible which we attribute to the rotational coupling between $(2)^2\Sigma^+$ and $(1)^2\Pi_{3/2}$ according to the coupling matrix in table 2. These give us additional information on this electronic state.

For each v_Σ level, only the two closest levels for each $^2\Pi$ component, with v_Π and v_Π', were selected, giving for each v_Σ and $J \geqslant 3/2$ a (5×5)-matrix. The actual level scheme for $(2)^2\Sigma^+$ and $(1)^2\Pi$, shown in figure 5, allowed to derive the level structure of the $^2\Pi$ state for six adjacent vibrational levels, labelled as $v_\Pi = 0$–5. We varied the Dunham coefficients for $(2)^2\Sigma^+$ and $(1)^2\Pi$, the coupling constants defined by expressions (8) and (9) and A_Π.

5. Results

First we analysed the coupling of the upper $^2\Sigma^+$ state to the state $^2\Pi_{1/2}$ only, because of the significant magnitude of spin-orbit coupling to this component with $\Omega = 1/2$. The perturbation for the presently assigned *e* levels appears at lower *J* than for the *f* levels. This is a clear confirmation that the assumed assignment of *e*/*f* (F_1/F_2) is correct because the rotational energy for the same *J* is higher for *f* than for *e* levels and the rotational constant of $(1)^2\Pi$ is larger than for $(2)^2\Sigma^+$.

For the remaining deviations, we found a regular series of localized (spanning 2 to 3 *J* levels) deviations, which could be undoubtedly assigned to the perturbation by the $^2\Pi_{3/2}$ state. Thus we extended the fit to the full size matrix 5×5 and also fitted the spin-orbit splitting A_Π of $(1)^2\Pi$.

We cover a large interval of rotational states and thus consider a *J*-dependence of the overlap integrals—or more specifically, the product of overlap integral and spin-orbit coupling—according to

$$V_{\Sigma\Pi}^{\text{fit}} = V_{\Sigma\Pi}^{\text{const}} + V_{\Sigma\Pi}^{J} \cdot J(J+1). \tag{10}$$

We do not have a solid theoretical basis for this analytic representation. Only for strong perturbations, the deviations are spread over a large range of *J* levels, namely for the overlap integrals $\langle v_\Pi | v_\Sigma \rangle$ with $\langle 0|3\rangle$, $\langle 1|2\rangle$ and $\langle 1|3\rangle$ (compare figure 6). Therefore, we introduced the *J*-dependence only for these perturbation pairs and got an improvement of the fit by almost a factor of two. The normalized standard deviation of the fit is $\sigma = 1.11$.

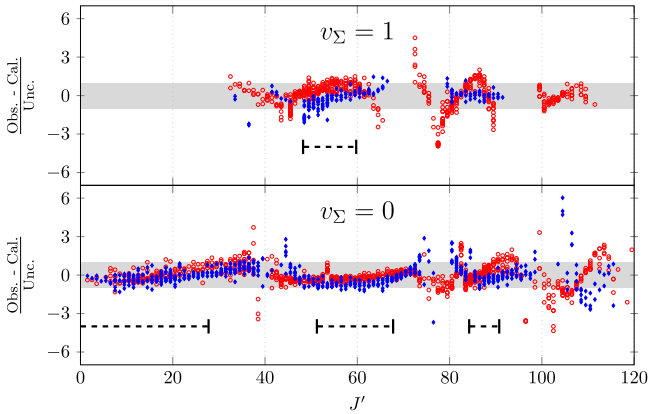

Figure 7. Deviation of observed level energies to those calculated with the deperturbation model, divided by the respective experimental uncertainty. Red circles indicate *e* levels and blue diamonds *f* levels. The grey region indicates the range of experimental uncertainty. Close to the perturbation centres, deviations of several times the experimental uncertainty appear. The dashed horizontal lines indicate the *J*-intervals that were sufficiently unperturbed to describe them with a Dunham series, whereas the other data could only be reproduced with the deperturbation model.

Figure 6 plots besides the observed perturbation energies for the two observed vibrational levels of $(2)^2\Sigma^+$ also as solid lines the calculated values from the fit. On the shown scale, there is no deviation visible between observation and calculation. The regular structure in the appearance of $^2\Pi_{1/2}$ and $^2\Pi_{3/2}$ perturbations when plotted over $J(J+1)$ is convincing evidence of the presented assignment of $^2\Pi_{1/2}$ and $^2\Pi_{3/2}$ crossings. Thus the observations also allow from the differences between the perturbations of the $\Omega = 1/2$ and $\Omega = 3/2$ components the determination of the spin-orbit splitting within the state $(1)^2\Pi$.

Figure 7 shows the relative deviations of observed level energies from energies predicted by the coupling model. The dashed lines in figure 7 mark the levels which were sufficiently unperturbed to be describable with a Dunham approach (equations (1) and (2)) within their experimental uncertainty. With the deperturbation model, most lines are well reproduced within their experimental uncertainty, however, the calculated lines near the perturbation centres do not fit the observed data similarly well. The stronger a level is perturbed, the lower is its $^2\Sigma^+$ amplitude and the lower is the intensity of a spectral line, because the transition dipole moment for $(1)^2\Pi$–$X(1)^2\Sigma^+$ transitions is much smaller than for $(2)^2\Sigma^+$–$X(1)^2\Sigma^+$ transitions [11, 13]. Due to this decreasing intensity and the expected large frequency shift (see figure 6), lines are more difficult to find and to assign in the spectrum, the closer they are to a perturbation centre.

With the deperturbation model, we were able to identify approximately 100 new lines that are considerably perturbed. However, there are still data gaps left at the perturbation centres.

The fitted molecular parameters are given in tables 3–5. In table 5, also the rotational quantum numbers for the

Table 3. Derived Dunham and spin-rotation parameters for the state $(2)^2\Sigma^+$ and the state $(1)^2\Pi$ of $^7Li^{88}Sr$. They give an accurate description for levels with $N \leqslant 119$, $v = 0, 1$ for state $(2)^2\Sigma^+$. The $(1)^2\Pi$ parameters describe the vibrational structure around the observed $(2)^2\Sigma^+$ levels with the assumed vibrational assignment $v_\Pi = 0$ to 5 for the deperturbation. Their absolute vibrational quantum numbers are not yet known. All values are given in cm^{-1}.

Y_{0n}	Y_{1n}	Y_{2n}	γ_{0n}	γ_{1n}	n
$(2)^2\Sigma^+$ Hund's case (a)					
$9.391\,98(14) \times 10^3$	$1.8151(27) \times 10^2$	—	$4.542(19) \times 10^{-2}$	$8.8(40) \times 10^{-4}$	0
$1.895\,36(25) \times 10^{-1}$	$-7.14(44) \times 10^{-4}$	—	$-8.16(50) \times 10^{-8}$	—	1
$-8.186(11) \times 10^{-7}$	$4.8(19) \times 10^{-9}$	—	—	—	2
$4.69(13) \times 10^{-12}$	—	—	—	—	3
$-2.59(98) \times 10^{-17}$	—	—	—	—	4
$(1)^2\Pi$ Hund's case (a)					
$8.2286(87) \times 10^3$	$2.7713(23) \times 10^2$	$-4.53(20) \times 10^0$	—	—	0
$2.621(35) \times 10^{-1}$	$-3.04(57) \times 10^{-3}$	—	—	—	1
$-1.43(45) \times 10^{-6}$	$-6.3(41) \times 10^{-8}$	—	—	—	2
$3.8(24) \times 10^{-11}$	—	—	—	—	3
$-1.85(62) \times 10^{-15}$	—	—	—	—	4

crossing of the $^2\Sigma^+$ and $^2\Pi_{1/2}$ levels are given for each pair of v_Σ and v_Π (compare figure 5) for getting the right order of magnitude for the J-dependence of the overlap integrals.

Since the actual quantum numbers v_Π are not known from the deperturbation process, the Dunham coefficients give only a local description for the $(1)^2\Pi$ levels, with the assumed vibrational range from $v_\Pi = 0$ to 5. The otherwise unobserved $(1)^2\Pi$ energy ladders cannot be expected to be predicted as well as those of the $(2)^2\Sigma^+$ state.

The deperturbation was achieved with a nonlinear fit, thus it is difficult to estimate how closely we approached the absolute minimum of the squared sum of the deviations. For the uncertainties of the parameters given in tables 3 and 4, we considered the development of these parameters during the course of our analysis period while adding more and more data. In this way, we consider the variances of the fit parameters under different sets of starting parameters so that the change of a given parameter over time gives a range of confidence. The relative uncertainties of the $(2)^2\Sigma^+$ Dunham parameters are generally one order of magnitude higher than of those from the linear fit in table 1. This is expected, since we constructed the $(2)^2\Sigma^+$ levels with the parameters from table 1 and the observed line frequencies with an assumed uncertainty near the Doppler width. Further, the uncertainties in table 1 are probably underestimated (see the discussion in section 3). The relative uncertainties of the $(1)^2\Pi$ parameters are mostly two orders of magnitude larger than for the $X(1)^2\Sigma^+$ parameters. This is due to the indirect observation of $(1)^2\Pi$ levels bia perturbations of the $(2)^2\Sigma^+$ levels and the above-mentioned missing lines near the perturbation centres. The relative uncertainty of the coupling parameters in table 4 were estimated in the same way. The spin-orbit constant A_Π is fairly well determined by the deperturbation because it results from the differences of the rotational ladders of $(1)^2\Pi_{1/2}$ and $(1)^2\Pi_{3/2}$.

The effective overlap integrals in table 5 have a numerical sensitivity of within the fourth digit shown in the table,

Table 4. Fitted coupling parameters of the $(2)^2\Sigma^+$–$(1)^2\Pi$ system. The magnitude of the $^2\Sigma^+$–$^2\Pi_{1/2}$-coupling is scaled with the overlap integrals given in table 5. See the text for details.

Parameter	Value
$B_{\Sigma\Pi}/(A_{\Sigma\Pi} - \gamma_{\Sigma\Pi})$	0.000 196(60)
$A_{\Pi\ (cm^{-1})}$	155.68(78)

which was checked by varying them by hand. But physically they are probably only good up to 1% because we have to consider significant correlation between them. We give their values with five significant figures, with which our calculations can safely be reproduced.

6. Discussion and outlook

The effective overlap integrals $V_{\Sigma\Pi}^{fit}$ scale the perturbation strength for individual crossings of v_Σ and v_Π level systems. These overlap integrals were treated as simple fit parameters in our model but they are effectively products of overlap integrals and the spin-orbit interaction. To untangle the different factors in the off-diagonal matrix elements, we took the opportunity that we derived several such products which have one constant, namely the spin-orbit parameter, in common. Therefore, the variation from vibrational pair to vibrational pair reflects the variation of the true overlap integrals. For the comparison between observation and theory, we applied the potentials from *ab initio* calculations from Pototschnig *et al* [16], calculated the overlap integrals $\langle 0|5\rangle$ to $\langle 0|20\rangle$ and $\langle 1|5\rangle$ to $\langle 1|20\rangle$ and compared the distribution with that of the fitted overlap integrals $V_{\Sigma\Pi}^{fit}$ in table 5. We found a good agreement of the two distributions when shifting our assumed vibrational quantum number by +12. This offset of vibrational quantum numbers also fits well to the energy range of vibrational $(1)^2\Pi$ levels that cross with the lowest two vibrational $(2)^2\Sigma^+$ levels

Table 5. Overlap integrals $V_{\Sigma\Pi}^{\mathrm{fit}}$ between the $(2)^2\Sigma^+$ and $(1)^2\Pi$ states from the deperturbation. The overlap integrals have units of (cm^{-1}), because they contain the spin-orbit interaction. The left and right values are $V_{\Sigma\Pi}^{\mathrm{const}}$ and $V_{\Sigma\Pi}^{J}$ according to equation (10). See the text for an estimate of the uncertainties. We also give the quantum numbers J closest to the crossing of $^2\Pi_{1/2}$ levels with the e and f $^2\Sigma^+$ levels. 'x' indicates that the crossing is beyond our data range (compare figure 5).

v_Π	$v_\Sigma = 0$		J		$v_\Sigma = 1$		J	
	$V_{\Sigma\Pi}^{\mathrm{const}}$	$V_{\Sigma\Pi}^{J}$	e	f	$V_{\Sigma\Pi}^{\mathrm{const}}$	$V_{\Sigma\Pi}^{J}$	e	f
0	3.5869[a]	—	x	x	3.5869[a]	—	x	x
1	1.8498	—	117 1/2	119 1/2	3.5869[a]	—	x	
2	6.3015	$4.123\,3 \times 10^{-4}$	97 1/2	100 1/2	2.8782	9.8436×10^{-4}	113 1/2	116 1/2
3	5.2871	—	74 1/2	76 1/2	2.0611	5.3282×10^{-4}	93 1/2	96 1/2
4	2.5188	—	39 1/2	42 1/2	1.4468	—	68 1/2	72 1/2
5	7.3432×10^{-3}	—	x	x	7.4308	—	27 1/2	30 1/2

[a] These parameters were kept fixed during the fit.

Table 6. Comparison of measured spectroscopic constants of ^{7}Li^{88}Sr with results of the Graz group [13, 16] (MRCI), converted to ^{7}Li^{88}Sr. For $(1)^2\Pi$ state, we calculated the parameters for $v_\Pi = 12$ from the *ab initio* potenial and compare these with $v = 0$ of our local description. All values are given in cm^{-1} except R_e, which is given in Å.

	R_e	$\omega_e \approx \mathrm{Y}_{10}$	$B_e \approx \mathrm{Y}_{01}$	T_e		
$X(1)^2\Sigma^+$	3.574	179.1	—	0		*ab initio*
	3.5405[a]	183.07	0.2074	0		this work
$(2)^2\Sigma^+$	3.728	183.0	—	9375		*ab initio*
	3.704[a]	181.51	0.1895	9391.98		this work
	R_e	$E_{v=13} - E_{v=12}$	B_{12}	$E_{v=12}$	A_Π	
$(1)^2\Pi$	3.130	241	0.32	8258	117.85[b]	*ab initio*
	—	277.12	0.2621	8366.0	155.68	this work

[a] Calculated from Y_{01}.
[b] Taken from [11] (SO-MS-CASPT2). The molecular constants of [13] and [11] agree within ca. 10%.

according to the calculations by Pototschnig *et al* and shows that the calculated energy difference between the two *ab initio* potentials is in no conflict with our observations. It should be noted that the J-dependent contributions to the overlap integrals in table 5 increase with J, whereas the corresponding *ab initio* overlap integrals get slightly smaller with increasing J. The fitted values of the J-dependent overlap integrals (equation (10)) therefore likely contain contributions of other J-dependencies, e.g. the spin-orbit coupling itself.

The comparison with the *ab initio* work leads to a scaling factor for the overlap integrals of

$$\frac{V_{\Sigma\Pi}^{\mathrm{fit}}}{V_{\Sigma\Pi}^{\mathrm{calc}}} \approx 302, \tag{11}$$

assuming the shift of 12 units in v_Π. With this, we can estimate now the spin-orbit coupling with equation (8). We assumed $p = \sqrt{2}$ as an approximation for a *sp*-atom pair from the atomic asymptote of the electronic molecular states in question (see figure 1) and $V_{\Sigma\Pi}^{\mathrm{calc}} = V_{\Sigma\Pi}$ for obtaining

$$A_{\Sigma\Pi} \approx \frac{V_{\Sigma\Pi}^{\mathrm{fit}}}{V_{\Sigma\Pi}^{\mathrm{calc}}} \frac{1}{\sqrt{2}} = (214 \pm 38)\ \mathrm{cm}^{-1}. \tag{12}$$

We neglect here the influence of the spin-rotation contribution in the non-diagonal matrix element. The value of $A_{\Sigma\Pi}$ is close to the magnitude of the molecular splitting constant A_Π (see table 4) and the spin-orbit constant A_{Sr} from the atomic asymptote with Sr $5p^3$P (see [19]). This might indicate that the value of p is slightly smaller than $\sqrt{2}$. Analogously, we get with equations (8) and (9)

$$B_{\Sigma\Pi} = 0.042\,8(51)\ \mathrm{cm}^{-1}, \tag{13}$$

while the *ab initio* potentials yields for $B_{\Sigma\Pi} = \langle v_\Sigma | \hbar^2/(2\mu R^2) | v_\Pi \rangle$, with relevant v_Σ and v_Π, values from 0.018 to 0.066 cm^{-1}. Our approach to factor out the overlap integral by assuming the other factors are independent of v seems to be a sufficient approximation for getting consistent coupling parameters and it indicates that the potential scheme from *ab initio* results is well applicable for this detailed analysis.

In table 6, we compare derived molecular constants with those of Pototschnig *et al*, whose work we already used for the vibrational analysis of the $(1)^2\Pi$ state. The comparison in table 6 shows a good general agreement between the calculations and our observations, with deviations of a few percent. For the $(1)^2\Pi$ constants, there are larger differences than for the $^2\Sigma^+$ constants. We could model the $(1)^2\Pi$ levels only indirectly, whereas the $^2\Sigma^+$ levels could be observed directly. The other *ab initio* calculations [1, 9–12, 14] come to similar results. The value of A_Π is higher by 30% compared to the

ab initio result by Gopakumar *et al* [11] and is about 3/4 of the atomic value A_{Sr}, which indicates that the $(1)^2\Pi$ state has a large contribution from the 5*p* electron of Sr. For such a comparison, it would be good to obtain a deeper insight into the eigenvectors derived in the *ab initio* calculation.

In the thermal emission spectrum, other vibrational bands than (0–0), (1–1), (1–0) and (1–2) are visible but too weak for rotational analysis (see figure 2). The fitted Dunham coefficients in tables 1 and 3 reproduce the $(2)^2\Sigma^+$–$X(1)^2\Sigma^+$ band heads with $v \leqslant 3$ of both $^2\Sigma^+$ states within 3 cm^{-1}. This means an extrapolation of two vibrational quanta. We identified the bands in figure 2 with these parameters. Since the $(2)^2\Sigma^+$ coefficients come from a fit of coupled electronic states, the coupling model has to be extended to describe the spectrum reliably over a wider range.

Higher vibrational $X(1)^2\Sigma^+$ levels are needed for a more complete description of the $X(1)^2\Sigma^+$ potential energy curve with the final goal to allow for the description of cold atomic collisions. The thermal emission spectrum, recorded around 1000 °C, shows distinct bands only for the four lowest vibrational levels of both the $(2)^2\Sigma^+$ and the $X(1)^2\Sigma^+$ states. This, together with the predicted distribution of Franck-Condon factors [13], leads us to conclude that the experimental methods deployed here will not allow us to observe much higher $X(1)^2\Sigma^+$ levels. To achieve a full description of the electronic ground state, other electronic transitions (e.g. (3) $^2\Sigma^+$–$X(1)^2\Sigma^+$) have to be used. Such transitions, with different Franck-Condon factors, could allow to address intermediate or high vibrational $X(1)^2\Sigma^+$ levels which could be used to interpolate the energy structure. But one encounters a significant problem, namely the overlap of the desired spectrum with strong spectra of the diatomic alkali metals also formed in the heat pipe.

A description of the $(2)^2\Sigma^+$–$(1)^2\Pi$ coupling with fitted potential energy curves would allow to greatly reduce the number of fit parameters since these curves provide both energy levels and overlap integrals. Such curves represent a global description of the electronic states. Because we only incorporated a few high vibrational $(1)^2\Pi$ levels, there is too much ambiguity regarding the shape of the $(1)^2\Pi$ potential energy curve to describe the perturbation with such a model. Like for the ground state, this problem can be overcome by extending the energy level data via observations of transitions to other electronic states which might fluoresce to the manifold of the $(1)^2\Pi$ state.

Acknowledgments

This work received financial support from the Deutsche Forschungsgemeinschaft (Grants No. TI 106/17-1 and No. OS 401/15-1).

ORCID iDs

Erik Schwanke https://orcid.org/0000-0002-9607-0753
Eberhard Tiemann https://orcid.org/0000-0002-4690-7738

References

[1] Gopakumar G, Abe M, Kajita M and Hada M 2011 *Phys. Rev.* A **84** 062514
[2] Krois G, Lackner F, Pototschnig J V, Buchsteiner T and Ernst W E 2014 *Phys. Chem. Chem. Phys.* **16** 22373
[3] Bruni C and Görlitz A 2016 *Phys. Rev.* A **94** 022503
[4] Guttridge A, Frye M D, Yang B C, Hutson J M and Cornish S L 2018 *Phys. Rev.* A **98** 022707
[5] Ciamei A *et al* 2018 *Phys. Chem. Chem. Phys.* **20** 26221
[6] Kajita M, Gopakumar G, Abe M and Hada M 2013 *J. Phys. B: At. Mol. Opt. Phys.* **46** 025001
[7] Yao J, Zhai H and Zhang R 2019 *Phys. Rev.* A **99** 010701
[8] Micheli A, Brennen G K and Zoller P 2006 *Nat. Phys.* **2** 341
[9] Guérout R, Aymar M and Dulieu O 2010 *Phys. Rev.* A **82** 042508
[10] Kotochigova S, Petrov A, Linnik M, Kłos J and Julienne P S 2011 *J. Chem. Phys.* **135** 164108
[11] Gopakumar G, Abe M, Hada M and Kajita M 2013 *J. Chem. Phys.* **138** 194307
[12] Pototschnig J V, Hauser A W and Ernst W E 2016 *Phys. Chem. Chem. Phys.* **18** 5964
[13] Pototschnig J V, Meyer R, Hauser A W and Ernst W E 2017a *Phys. Rev.* A **95** 022501
[14] Zeid I, Atallah T, Kontar S, Chmaisani W, El-Kork N and Korek M 2018 *Comput. Theor. Chem.* **1126** 16
[15] Schwanke E, Knöckel H, Stein A, Pashov A, Ospelkaus S and Tiemann E 2017 *J. Phys. B: At. Mol. Opt. Phys.* **50** 235103
[16] Pototschnig J V, Meyer R, Hauser A W and Ernst W E 2017 (personal communication)
[17] Lefebvre-Brion H and Field R W 1986 *Perturbations in the Spectra of Diatomic Molecules* (New York: Academic)
[18] James F and Roos M 1975 *Comput. Phys. Commun.* **10** 343
[19] Sansonetti J 2013 *Handbook of Basic Atomic Spectroscopic Data* NIST Standard Reference Database 108 (https://nist.gov/pml/handbook-basic-atomic-spectroscopic-data) (https://doi.org/10.18434/T4FW23) (Accessed: 2 Feb 2019)